

# Soft Microfluidic Assemblies of Sensors, Circuits, and Radios for the Skin

Sheng Xu,<sup>1\*</sup> Yihui Zhang,<sup>2,3\*</sup> Lin Jia,<sup>1\*</sup> Kyle E. Mathewson,<sup>4\*</sup> Kyung-In Jang,<sup>1</sup> Jeonghyun Kim,<sup>1,6</sup> Haoran Fu,<sup>2,5</sup> Xian Huang,<sup>1</sup> Pranav Chava,<sup>1</sup> Renhan Wang,<sup>1</sup> Sanat Bhole,<sup>1</sup> Lizhe Wang,<sup>1</sup> Yoon Joo Na,<sup>1</sup> Yue Guan,<sup>1</sup> Matthew Flavin,<sup>1</sup> Zhesen Han,<sup>1</sup> Yonggang Huang,<sup>2†</sup> John A. Rogers<sup>1,4†</sup>

When mounted on the skin, modern sensors, circuits, radios, and power supply systems have the potential to provide clinical-quality health monitoring capabilities for continuous use, beyond the confines of traditional hospital or laboratory facilities. The most well-developed component technologies are, however, broadly available only in hard, planar formats. As a result, existing options in system design are unable to effectively accommodate integration with the soft, textured, curvilinear, and time-dynamic surfaces of the skin. Here, we describe experimental and theoretical approaches for using ideas in soft microfluidics, structured adhesive surfaces, and controlled mechanical buckling to achieve ultralow modulus, highly stretchable systems that incorporate assemblies of high-modulus, rigid, state-of-the-art functional elements. The outcome is a thin, conformable device technology that can softly laminate onto the surface of the skin to enable advanced, multifunctional operation for physiological monitoring in a wireless mode.

Continuous physiological monitoring and intervention are needed for the treatment of many medical conditions. Multimodal, noninvasive access to the body can be accomplished through cutaneous electrical/optical/fluidic interfaces. “Skin-like” devices, sometimes referred to as “epidermal” electronic systems (*1, 2*), offer thicknesses (*3–5*), moduli, levels of elastic stretchability, and other basic physical properties that match those of the skin itself so as to allow a soft, compliant type of integration. Recent work demonstrates that such characteristics can be achieved by exploiting ultrathin geometries (*1, 6, 7*), soft active materials (*3, 4, 8–13*), and/or liquid metals (*14–16*). Here, we demonstrate ideas that expand options beyond these specialized approaches to include commercial, chip-scale components, ranging from integrated circuits, to radio frequency hardware, microelectromechanical structures, physical/chemical sensors, and power sources. The key concept involves microfluidic suspensions of interconnected assemblies of such chips

in thin elastomeric enclosures to enable soft, low-modulus mechanics at the system level. Here, the high-modulus components have little impact on the overall mechanics, even when they are present at high areal coverage. For otherwise similar device layouts, this strategy improves the mechanical compliance and the stretchability by orders of magnitude compared with those possible using previous approaches that incorporate chip-scale components (*17–20*). The resulting systems can laminate softly and noninvasively onto the skin to define highly functional interfaces with the ability to combine unusual elements with standard parts. These concepts enable broad classes of sophisticated bio-integrated electronic devices, as illustrated here through systems that offer wirelessly powered operation and precision measurement of biopotentials, acceleration, and/or temperature, with radio frequency (RF) data transmission.

The layout involves a matrix of microfluidic spaces designed to decouple the mechanics of the constituent devices and associated interconnect network from a thin, elastomeric enclosure that simultaneously provides a supporting surface (substrate) and an encapsulation layer (superstrate). Each component selectively bonds to the bottom surface of this enclosure at small, localized cylindrical features of relief (support posts) molded onto the thin elastomer substrate. Except for these posts, the devices are suspended in the surrounding fluid and, as a result, are mechanically isolated. A free-floating network of serpentine-shaped interconnects with multilayer, neutral mechanical plane layouts joins the devices into circuit architectures that provide system-level function. Presented in Fig. 1A is an exploded view schematic illustration

of an integrated device capable of acquisition, filtering, amplification, and RF transmission of electrophysiological (EP) data, for precision measurement of electrocardiograms (ECGs), electromyograms (EMGs), electrooculograms (EOGs), and electroencephalograms (EEGs).

Bonding the superstrate and substrate at their edges defines a microfluidic structure that is subsequently filled with a dielectric fluid by use of an injection needle (Fig. 1B and fig. S1). Selection criteria for the fluid include (i) wettability toward the electronic components and the substrate/superstrate to facilitate the filling process, (ii) large volume resistivity ( $>1 \times 10^{14} \text{ Ohm} \cdot \text{cm}$ ) to eliminate electrical crosstalk, (iii) high dielectric strength ( $>10 \text{ kV/mm}$ ) to avoid electrical breakdown, (iv) moderate viscosity ( $\sim 5 \text{ Pa} \cdot \text{s}$ ) to enhance impact resistance, (v) good thermal stability [weight loss  $< 0.5\%$  at  $100^\circ\text{C}$  for 4 hours (fig. S2)] to allow reliable long-term operation, (vi) low-loss RF properties and small dielectric constant ( $< 3$ ) to minimize influence on RF operation, (vii) low reactivity and chemical stability to avoid corrosion or other forms of chemical degradation, (viii) hydrophobic character to expel moisture from the package, and (ix) optical transparency to enable rapid inspection of the components. The devices reported here use a soft, silicone elastomer (Ecoflex, Smooth-On, Easton, Pennsylvania) for the substrate/superstrate, and a high-molecular-weight silicone oligomer (Sylgard 184, without curing agent) for the fluid.

The free-floating interconnects can buckle, twist, and deform with little constraint, both in and out of the plane, in response to externally imposed deformations of the entire system. Likewise, the fluid-based strain isolation strategy allows large-range motions of the substrate/superstrate with minimal coupling to the device components. This mechanics are apparent from the three-dimensional (3D) finite element analysis (FEA) results of Fig. 1C. The ability of the interconnects to move freely increases their range of stretchability, relative to designs that involve bonding to or embedding in solid or porous elastomers (*17–23*). For the case of an interconnect shown in Fig. 1C, this increase in stretchability corresponds to a factor of  $\sim 10$  or  $\sim 20$  when compared with the case of bonding or embedding, respectively (fig. S3). The maximum principal strain in the interconnect metal (Fig. 1C) is less than  $\sim 0.2\%$  for a biaxial stretch of 50% for the entire system. The support posts lead to differences in absolute strains between the hard components and the elastomer immediately below, which can be as large as  $\sim 64\%$  for the same level (50%) of biaxial stretch.

A dense array of sharp, pyramidal features molded onto the substrate prevent nonspecific adhesion to the interconnects and the devices, to allow low-friction, lubricated relative motions. The cross-sectional scanning electron microscope (SEM) images of Fig. 1D and fig. S4 show this relief, as well as that associated with a support post to allow strain isolation of component chips

<sup>1</sup>Department of Materials Science and Engineering and Frederick Seitz Materials Research Laboratory, University of Illinois at Urbana-Champaign, Urbana, IL 61801, USA. <sup>2</sup>Department of Mechanical Engineering and Department of Civil and Environmental Engineering, Center for Engineering and Health, and Skin Disease Research Center, Northwestern University, Evanston, IL 60208, USA. <sup>3</sup>Center for Mechanics and Materials, Tsinghua University, Beijing, 100084, P.R. China. <sup>4</sup>Beckman Institute for Advanced Science and Technology, University of Illinois at Urbana-Champaign, Urbana, IL 61801, USA. <sup>5</sup>Department of Civil Engineering and Architecture, Zhejiang University, Hangzhou 310058, P.R. China. <sup>6</sup>Department of Materials Science and Engineering, Department of Energy Engineering, Hanyang University, Seoul 133-791, Republic of Korea.

\*These authors contributed equally to this work.

†Corresponding author. E-mail: jrogers@illinois.edu (J.A.R.); y-huang@northwestern.edu (Y.H.)

and a physical barrier to prevent entanglement of adjacent interconnects. The same region after integration of the interconnect network by transfer printing appears in Fig. 1, E and F. The chips [all <1 mm in thickness, achieved with mechanical grinding (fig. S5)] bond electrically and mechanically to this network via a low-temperature solder (figs. S6 and S7 and movie S1). Wide, straight traces (fig. S8) pass through opposite edges of the microfluidic enclosure (microfluidic thickness, ~1 mm; superstrate thickness, ~0.1 mm) and terminate at external contact pads that provide

locations for lamination of epidermal electrodes (fig. S9) as interfaces to the skin. The completed system (Fig. 1G) includes modules for (i) wireless power supply through resonant inductive energy transfer, (ii) low-noise amplification and filtering of EP signals, and (iii) frequency-modulated RF transmission of measured data. The components and the design rationale are summarized in table S1 and fig. S10. The abilities of the device to stretch (shown here to ~30% uniaxial strain) and twist (shown here to ~75°) are evident from images in Fig. 1, H and I, respectively. Details

on the materials and fabrication procedures are available as supplementary materials on *Science* Online.

Mechanical behaviors at the system level are important to overall design. Summarized in Fig. 2 are systematic computational and experimental studies of the device in Fig. 1, without the superstrate membrane to facilitate imaging. 3D-FEA results (Fig. 2A) and experimental pictures (Fig. 2B) reveal the configurations of the chips and interconnects at various levels of equal-biaxial stretch. The good agreement validates the models

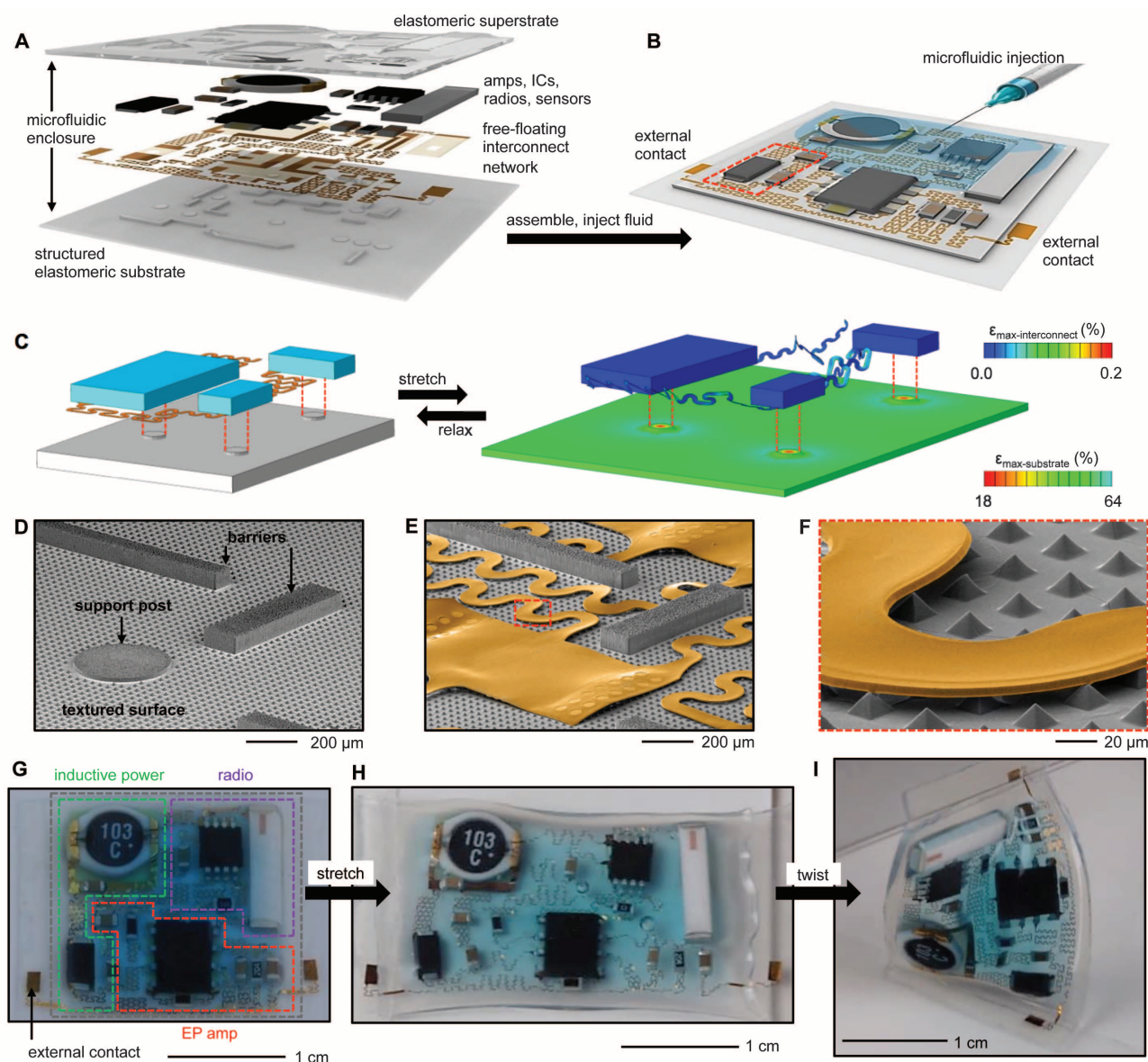


**Fig. 1. Schematic illustrations, SEMs, and pictures of a soft, stretchable electronic system that integrates strain-isolated device components and a free-floating interconnect network in a thin elastomeric microfluidic enclosure.** (A) Exploded-view schematic illustration of the key components of the system. (B) Illustration of the system after assembly, during initial stages of microfluidic injection using a syringe. (C) 3D-FEA results, in exploded-view format, that show the mechanics associated with equal-biaxial stretching of a small region of this system, as indicated by the red dash box in (B). The colors indicate the maximum principal strains. The buckling physics of the free-floating

serpentine interconnects and the strain isolation mechanics of the suspended chips represent the key features. (D) Angled-view SEM of a region of the substrate showing a textured surface with different structures labeled. (E) Angled-view SEM of the same region in (D), after transfer printing the interconnect network (yellow). (F) Angled-view SEM of the region of (E) indicated by the red dashed box. (G) Image of a system with the colored dashed boxes and labels to identify the various subsystems. The gray dashed box around the periphery indicates, approximately, the location of bonding of the superstrate. (H and I) Image of this system in a (H) stretched and (I) twisted configuration.



and establishes their utility as design tools for optimizing the layouts of the chips and the shapes of the interconnects. In particular, for any choice of system geometry the computed results allow rapid identification of locations of (i) high principal strains, (ii) entanglements in the interconnects, and (iii) collisions between the chips. An iterative process that involves coupled considerations in circuit and mechanics design, with 3D-FEA modeling as a guide, allows optimization of all relevant parameters (including positions of molded barriers) for a desired device size, degree of stretchability, and effective modulus. The system shown here results from several iterations in the layouts of the chips and the geometries of the self-similar serpentine shapes that form the aperiodic interconnection network. Attention to the hierarchical mechanics of in- and out-of-plane bending and

twisting in the serpentine and their dependence on geometry is paramount, subject to constraints set by requirements on their electrical properties. The subtle effects that can occur are shown in Fig. 2C and fig. S11. An example of one of the many modifications introduced with guidance from theory is a small bonding site added at the midpoint of the long interconnect at the base edge so as to ensure reversibility in its mechanics and to avoid entanglements (fig. S7). The final design offers an effective modulus, at the system level, that is only slightly larger (by 3 to 5%) than the intrinsic value associated with the bare elastomeric substrate (table S2). Uniaxial testing of the substrate with and without the chips, interconnect network, and surrounding fluid reveal almost identical stress/strain responses, as shown in the bottom frame of Fig. 2B. This outcome is notable,

considering the large differences between the moduli of the electronic materials ( $\sim 100$  GPa) and the elastomers ( $\sim 180$  kPa).

In addition to a low modulus, the system offers a large range of stretchability. For example, 100% equal-biaxial strain induces maximum principal strains of only  $\sim 2\%$  in the active materials (Cu of the interconnects), as highlighted by a segment of the interconnect network shown in the bottom frame of Fig. 2A. The maximum biaxial stretchability predicted with 3D-FEA is  $\sim 125\%$ , limited by localized fracture of the Cu (failure strain  $\sim 5\%$ ) in the interconnect network, which is consistent with experimental observation ( $\sim 100\%$ ). Reversible, elastic behaviors can be obtained (yield strain of Cu,  $\sim 0.3\%$ ) for biaxial strains of  $\sim 49\%$  (fig. S12), even with the high ( $\sim 46\%$ ) cumulative areal coverage of chips

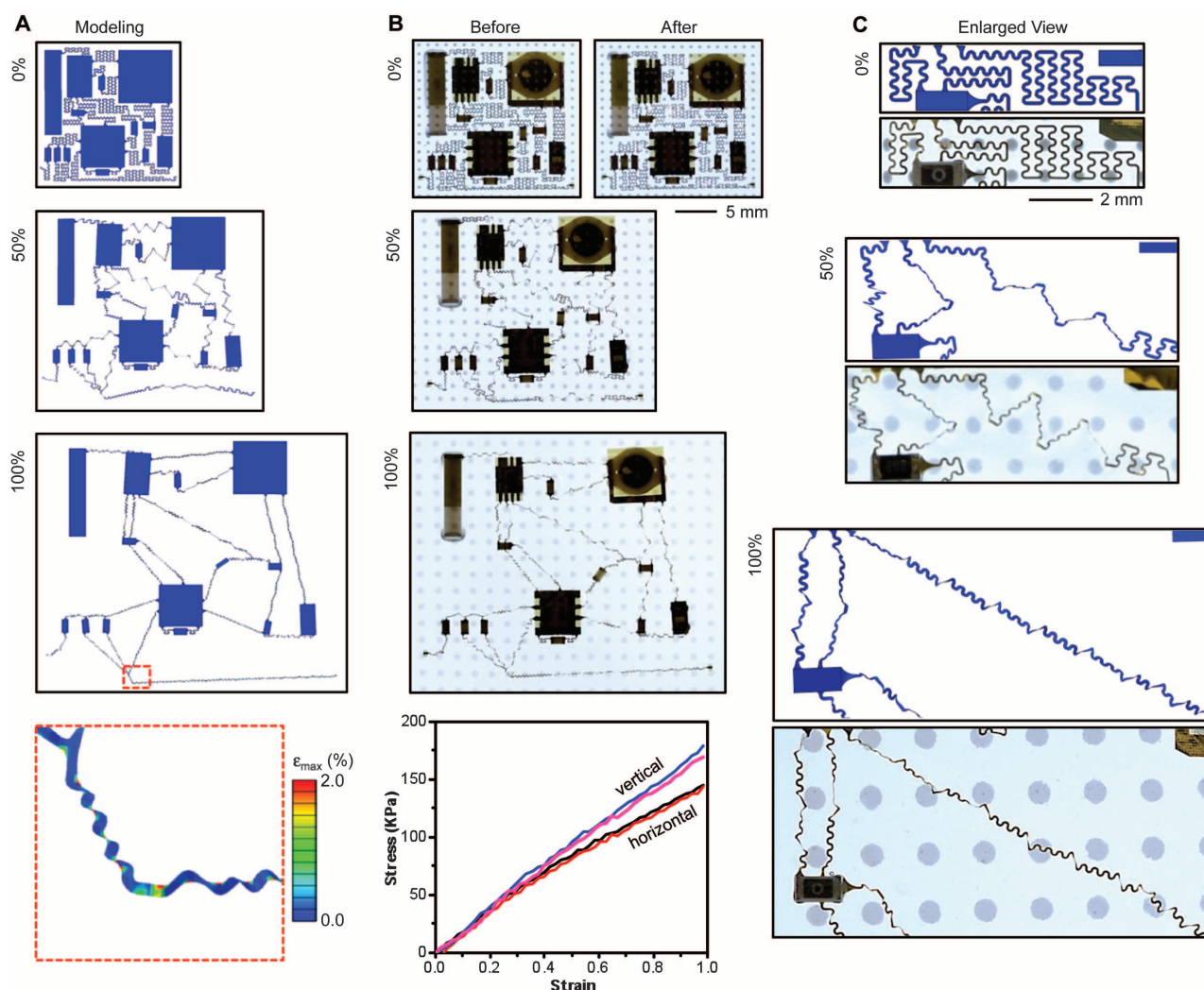


**Fig. 2. Computational and experimental studies of the physics of buckling in free-floating interconnect networks and of strain isolation in suspended chips for a wireless EP sensor.** (A) System-level 3D-FEA results for various magnitudes of equal-biaxial tensile strain. The color shows the maximum principal strains across each part of the system. (Bottom) Illustration of a small region of the interconnect network. (B) Optical images of the device at equal-biaxial strains that correspond to those evaluated by

3D-FEA. An additional image shows the system after release of the strain, to illustrate reversibility in the responses. (Bottom) Graph of the stress/strain responses measured by uniaxial testing for the case of a system with (black, in horizontal; blue, in vertical) and without (red, in horizontal; pink, in vertical) the chips and interconnect network. The results indicate nearly complete decoupling of the mechanics of the chips and interconnects from the substrate. (C) Images and 3D-FEA results for a local region.

in this device layout. Practical limits in uniaxial stretching are  $\sim 40\%$ , defined by collisions of adjacent chips caused by orthogonal contractions that arise from the Poisson effect (figs. S13 and S14). The device can be cycled for more than 6000 times under 30% uniaxial strain at a frequency of 0.6 Hz (fig. S15) without degradation. In all cases, deformations in the substrate show no evidence of constraints in motion associated with the chips or the interconnect network, as illustrated by the uniform separations between fiducial dots (Cr, 100 nm thick) deposited in a square array on the back surface of the substrate, which is visible in the images of Fig. 2. Quantitative analysis is provided in fig. S16. This low-modulus [ $\sim 180$  kPa, as soft as the skin (*1*)],

isotropic stretchable response follows from the microfluidic strain-isolation approaches. Analogous systems that do not exploit selective bonding of the chips to support posts show highly nonuniform deformations in the substrate (fig. S17); those that replace the microfluidics with solid elastomer show an elastic stretchability of only 6% and local effective moduli that vary from values comparable with those of the chips themselves ( $>100$  GPa) to the elastomer constrained by the bonded interconnects ( $\sim 250$  kPa). Such characteristics are poorly matched to requirements for mounting on the skin.

Shown in Fig. 3, A and B, is a completed device ( $\sim 1.7 \times 1.8$  cm<sup>2</sup>) that includes a pair of epidermal electrodes (each  $\sim 0.8 \times 1$  cm<sup>2</sup>, in fila-

mentary, self-similar serpentine mesh designs) (fig. S18) laminated onto the skin of the forearm, in undeformed and deformed states, respectively. Here, low interface stresses associated with the low effective modulus of the device enable robust adhesion to the skin through van der Waals forces alone, facilitated by an ultralow modulus thin elastomer coating on the bottom surface of the substrate. Alternating voltage (150 kHz) applied to a primary coil in proximity (within millimeters) to the device activates it by creating direct current output from the inductive power module. The total power consumption is  $\sim 35$  mW. Laminating the device across the sternum with the electrodes in bilateral fourth intercostal spaces enables wireless ( $\sim 2.4$  GHz) collection of ECG (movie S2) at distances of up to 1 m (fig. S19). The data show excellent signal-to-noise ratios, with clearly identifiable sequences of Q, R, and S waveforms (Fig. 3C). The fidelity of this system is similar to that of conventional commercial hardware with wired connections (fig. S20). Even weak electrophysiological signals can be captured effectively through EEG measured between electrodes on the forehead (positions Fpz and AF7), as illustrated in Fig. 3D, compared with signals simultaneously collected by using commercial hardware. Here, the subject engaged in mental math (counting backward by 7 from 200) for 1 min, closed his eyes, and remained at rest for another minute. EOG activity from the eyes closing separates the two tasks. The data reveal strong high-frequency activity during mental math and strong low-frequency activity during rest (fig. S21), as expected. Experimental details and many additional examples (fig. S22) appear in the supplementary materials.

The core concepts can also be used in multifunctional systems that allow not only EP sensing but also precision recording of motion with a triaxial accelerometer and with a thermal sensor, switched sequentially by a multiplexer (fig. S23). Such capabilities are important for applications that range from training in sports to tracking in sleep apnea studies, monitoring in neonatal care, and assessing cognitive state and awareness. The device in this case ( $1.9 \times 2.9$  cm<sup>2</sup>) includes 31 component chips and a complex, multilayer interconnect network. The components and design rationale are summarized in table S3 and fig. S24. At low duty cycle operation (fig. S25), the power consumption (few milliwatts) lies in a range that can be addressed not only with near-field communication, but also with a small coin-cell battery or, potentially, far-field RF power transfer. A pair of contact pads enables integration of these and other options in power supply (Fig. 4A and fig. S26). A combined circuit and mechanics iterative design process, similar to that described for the single-channel device, enables a high level of stretchability and low effective modulus. As a consequence, the system can naturally integrate with the skin and remain adhered through van der Waals forces during twisting, stretching, and pinching (Fig. 4B and fig. S27). An EMG

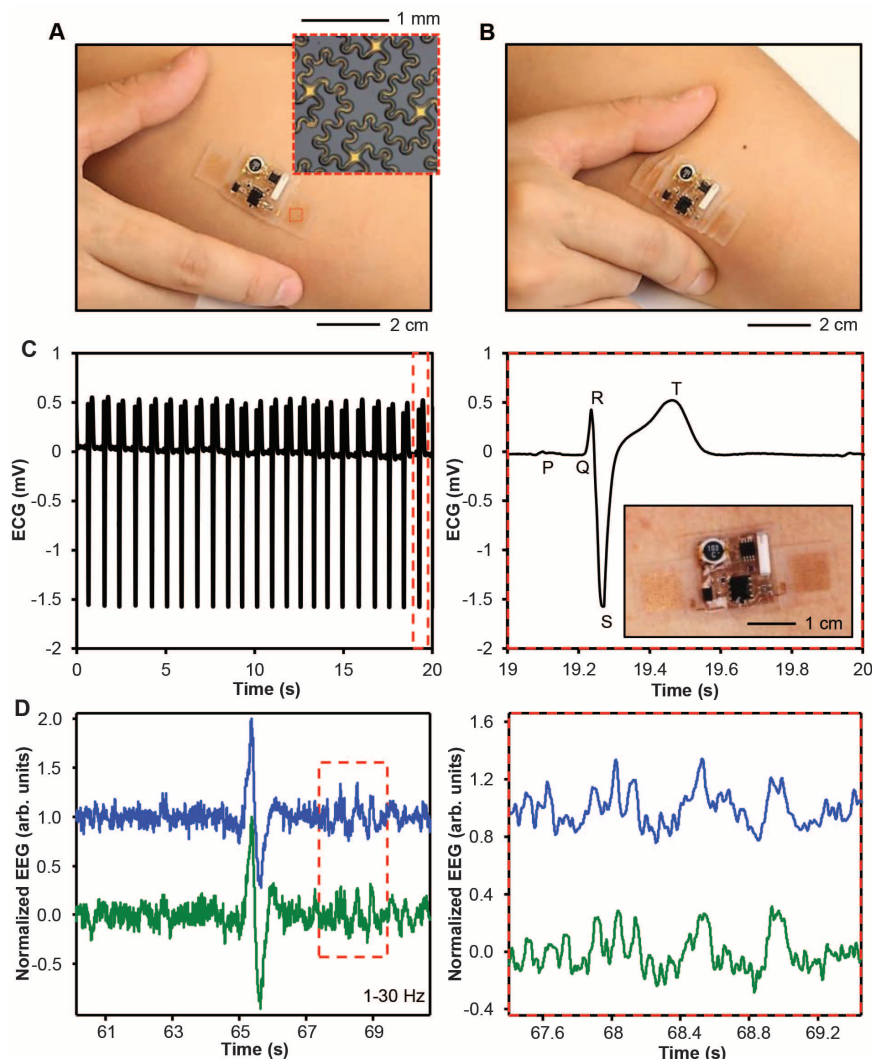


**Fig. 3. Images and operational data from a wireless EP sensor.** (A and B) Optical images of the device on the forearm, with a pair of epidermal electrodes in self-similar serpentine mesh layouts (inset optical micrograph) for an (A) undeformed state and (B) compressed and twisted state. (C) ECG acquired by using a device mounted on the sternum. The graph on the right provides a detailed view that shows the expected Q, R, and S waveforms. (D) EEG acquired from the left forehead during mental math and rest (green), and simultaneous measurement by using a wired commercial device (blue), mounted next to the wireless system. The large deflection represents the eyes closing as the subject shifts from mental math to resting, as shown in detail in the right plot. Data are plotted in arbitrary units, normalized and offset in the vertical direction to facilitate comparisons.



recorded from the forearm during repeated clenching and releasing of the fist is shown in Fig. 4C. The output of the accelerometer during walking and falling appears in Fig. 4D. The temperature responses induced through breathing onto the device (Fig. 4E) and physical exercise are consistent with those observed by using a commercial infrared camera (figs. S28 and S29).

The results presented here establish a general, quantitative experimental and theoretical framework for hard/soft composite systems that exploit (i) microfluidic suspensions to mechanically isolate rigid materials from compliant, elastomeric enclosures, (ii) topographical features and patterned surface chemistries to control interface adhesion, and (iii) self-similar structural designs to provide hierarchical buckling mechanics and large elastic strain range. Multifunctional devices that exploit these ideas allow mounting on the

skin in ways that are barely perceptible, in a mechanical sense. Additional possibilities include construction of hybrid systems that incorporate epidermal transistors for amplified, multiplexed addressing of signals from distributed arrays of soft sensors, with collections of strain-isolated, chip-scale components for data storage, processing, and RF transmission. Here, replacing the fluids with ultralow-modulus elastomers may capture some of the favorable mechanics and also eliminate the potential for leakage. Areas of potential use range from physiological status monitoring in neo-natal intensive care units to continuous assessment of responses to pharmaceuticals administered in the home, where existing technologies exert undue stresses and levels of discomfort on the patient. These directions—especially when pursued by using recent advances in power-efficient radios (24–26), wireless energy

transfer schemes (27–29) and functional microfluidics (14–16)—have potentially broad implications for the future of body-integrated electronics.

## References and Notes

1. D. H. Kim *et al.*, *Science* **333**, 838–843 (2011).
2. J.-W. Jeong *et al.*, *Adv. Mater.* **25**, 6839–6846 (2013).
3. M. Kaltenbrunner *et al.*, *Nature* **499**, 458–463 (2013).
4. M. S. White *et al.*, *Nat. Photonics* **7**, 811–816 (2013).
5. M. S. Mannoer *et al.*, *Nat. Commun.* **3**, 763 (2012).
6. J. A. Rogers, M. G. Lagally, R. G. Nuzzo, *Nature* **477**, 45–53 (2011).
7. C. F. Pan *et al.*, *Nat. Photonics* **7**, 752–758 (2013).
8. C. Wang *et al.*, *Nat. Mater.* **12**, 899–904 (2013).
9. S. C. B. Mannsfeld *et al.*, *Nat. Mater.* **9**, 859–864 (2010).
10. D. J. Lipomi *et al.*, *Nat. Nanotechnol.* **6**, 788–792 (2011).
11. T. Sekitani, T. Someya, *MRS Bull.* **37**, 236–245 (2012).
12. G. Schwartz *et al.*, *Nat. Commun.* **4**, 1859 (2013).
13. C. Keplinger *et al.*, *Science* **341**, 984–987 (2013).
14. M. Kubo *et al.*, *Adv. Mater.* **22**, 2749–2752 (2010).
15. E. Palleau, S. Reece, S. C. Desai, M. E. Smith, M. D. Dickey, *Adv. Mater.* **25**, 1589–1592 (2013).
16. D. M. Vogt, Y. L. Park, R. J. Wood, *IEEE Sens. J.* **13**, 4056–4064 (2013).
17. S. Wagner, S. Bauer, *MRS Bull.* **37**, 207–213 (2012).
18. T. Sterken *et al.*, *Conf. Proc. IEEE Eng. Med. Biol. Soc.* **2011**, 6886–6889 (2011).
19. F. Axaia *et al.*, *Conf. Proc. IEEE Eng. Med. Biol. Soc.* **2011**, 5687–5690 (2007).
20. M. Gonzalez *et al.*, *Microelectron. Reliab.* **51**, 1069–1076 (2011).
21. H. Vandeparre, Q. Liu, I. R. Mineev, Z. Suo, S. P. Lacour, *Adv. Mater.* **25**, 3117–3121 (2013).
22. A. Romeo, Q. H. Liu, Z. G. Suo, S. P. Lacour, *Appl. Phys. Lett.* **102**, 131904 (2013).
23. S. P. Lacour, S. Wagner, R. J. Narayan, T. Li, Z. G. Suo, *J. Appl. Phys.* **100**, 014913 (2006).
24. Y. Lee, B. Giridhar, Z. Foo, D. Sylvester, D. B. Blaauw, *IEEE J. Solid-State Circuits* **48**, 2511–2521 (2013).
25. Y. Lee *et al.*, *IEEE J. Solid-State Circuits* **48**, 229–243 (2013).
26. Y. Sun, H. Luo, S. K. Das, *IEEE Trans. Depend. Secure Comput.* **9**, 785–797 (2012).
27. E. Y. Chow, M. M. Morris, P. P. Irazoqui, *IEEE Microw. Mag.* **14**, 64–73 (2013).
28. S. Kim, J. S. Ho, A. S. Y. Poon, *Phys. Rev. Lett.* **110**, 203905 (2013).
29. S. J. Thomas, R. R. Harrison, A. Leonardo, M. S. Reynolds, *IEEE Trans. Biomed. Circuit Syst.* **6**, 424–436 (2012).

**Acknowledgments:** This work was supported by the U.S. Department of Energy, Office of Basic Energy Sciences, Division of Materials Sciences and Engineering under Award DE-FG02-07ER46471 through the Frederick Seitz Materials Research Laboratory at the University of Illinois at Urbana-Champaign, and the Korean Foundation for International Cooperation of Science and Technology (KICOS) through a grant [K207040000307A050000310, Global Research Laboratory (GRL) Program] provided by the Korean Ministry of Science and Technology (MOST). K.E.M. was supported by a postdoctoral fellowship from the Beckman Institute. The authors thank V. Malyarchuk, S. H. Ali, Y. Song, T. Banks, and S. Xiang for technical support and stimulating discussions.

## Supplementary Materials

[www.sciencemag.org/content/344/6179/70/suppl/DC1](http://www.sciencemag.org/content/344/6179/70/suppl/DC1)

Materials and Methods

Figs. S1 to S29

Tables S1 to S3

References (30, 31)

Movies S1 and S2

24 December 2013; accepted 4 March 2014

10.1126/science.1250169

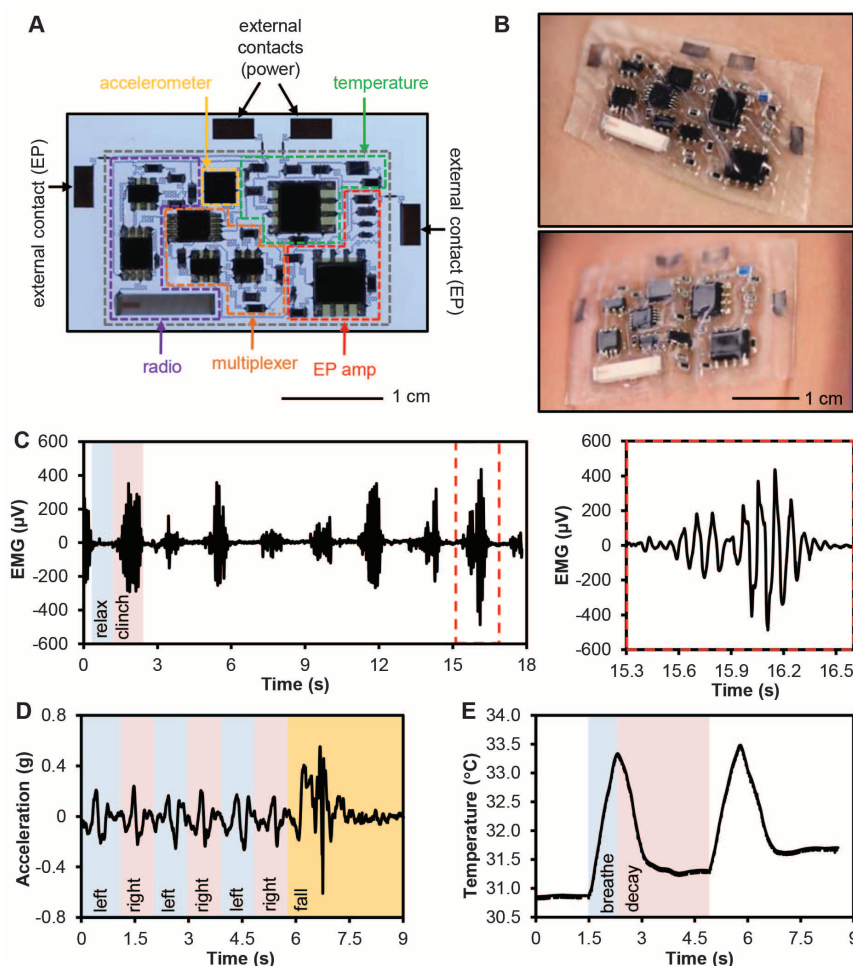


**Fig. 4. Images and operational data from a multifunctional wireless sensor.** (A) Optical image with colored dashed boxes and labels to identify the various subsystems. The gray dashed box around the periphery indicates, approximately, the location of bonding of the superstrate. (B) Images of the device on the skin in (top) twisted and stretched and (bottom) compressed states. (C) EMG acquired from above the left carpi radialis during periodic clenching and relaxing of the fist. (Right) An enlarged view of the EMG for a single clenching motion. (D) Acceleration profiles corresponding to walking, with the device mounted on the forearm. The data near the end of this timeframe corresponds to an intentional fall. (E) Temperature response to breathing warm air onto the device. The data shown in this figure were collected by use of a small coin cell battery as a source of power.